

Copper(I) complexes of phenanthrolineimidazole ligands: structures, photophysical properties, and quantum chemical studies

Sheng-Xian Xu¹ · Jing-Lan Wang¹ · Feng Zhao¹ ·
Hong-Ying Xia¹ · Yi-bo Wang²

Received: 15 June 2015 / Accepted: 17 July 2015 / Published online: 26 July 2015
© Springer International Publishing Switzerland 2015

Abstract Three copper(I) complexes, [Cu(PimP)(POP)]PF₆ (**1**), [Cu(NimP)(POP)]PF₆ (**2**), and [Cu(AimP)(POP)]PF₆ (**3**) (PimP = 2-phenyl-1*H*-imidazo[4,5-*f*][1,10]phenanthroline, NimP = 2-(2-naphthyl)-1*H*-imidazo[4,5-*f*]phenanthroline, AimP = 2-(9-anthryl)-1*H*-imidazo[4,5-*f*]phenanthroline, POP = bis[2-diphenylphosphino]-phenyl)ether) have been synthesized and characterized. Investigations into the effects of the varying substituents on the structural, absorption, and emission characteristics of the corresponding complexes are presented. Complexes **1** and **2** exhibit similar photophysical properties with the weaker lowest lying MLCT absorption at $\lambda > 400$ nm and the phosphorescence ³MLCT/³LLCT emission in the range of 570–590 nm, whereas complex **3** shows different absorption and emission properties, in which the LLCT absorption band is overlapped with the structured absorption bands belonging to the characteristic peaks of the anthracene moiety, and the emitting excited state is described as the ³LLCT character. Density functional theory and time-dependent density functional theory calculations were

employed to rationalize the photophysical properties of the complexes.

Introduction

Copper(I) complexes have attracted considerable attention since the pioneering work of McMillin et al. [1] on the photoluminescence properties of copper diimine complexes in the 1970s. Attractive features of Cu(I) complexes include their low cost and generally low toxicities. Furthermore, Cu(I) complexes show some photophysical properties similar to those of ruthenium(II) complexes, which are widely used for solar energy conversion, OLEDs, photocatalysis, and so on [2–4]. The two types of Cu(I) complexes most commonly investigated are the homoleptic [Cu(N[^]N)₂]⁺ type (where N[^]N denotes a diimine ligand) and the heteroleptic [Cu(N[^]N)(P[^]P)]⁺ type (where P[^]P denotes a bisphosphine ligand). [Cu(N[^]N)₂]⁺ complexes often show poor luminescent properties (low quantum yields and very short-lived lifetimes) [5, 6] because of the distortion of the complexes from tetrahedral (S₀ state) to the square planar geometry upon MLCT excitation, even when bulky substituents are introduced into the α positions relative to the coordinating nitrogen atoms [7]. The longest excited-state lifetimes reported to date for these complexes only range from 1 to 2.8 μ s, with moderate quantum yields of up to 6.3 % [8]. Compared to [Cu(N[^]N)₂]⁺ complexes, [Cu(N[^]N)(P[^]P)]⁺ complexes exhibit much superior photoluminescence properties. This is due to the introduction of the P[^]P ligand [9–11], not only due to its greater rigidity but also its ability to prevent solvent-induced exciplex quenching [12]. Among the most intensively studied complexes are the bis[(2-diphenylphosphino)-phenyl]ether (POP) containing

Electronic supplementary material The online version of this article (doi:10.1007/s11243-015-9967-5) contains supplementary material, which is available to authorized users.

✉ Feng Zhao
zhf19752003@163.com

✉ Hong-Ying Xia
xiahongying85@sohu.com

¹ School of Chemistry and Chemical Engineering, Jiangxi Science and Technology Normal University, Fenglin Street, Nanchang 330013, Jiangxi, People's Republic of China

² Key Laboratory of Guizhou High Performance Computational Chemistry, Department of Chemistry, Guizhou University, Guiyang 550025, People's Republic of China

$[\text{Cu}(\text{N}^{\wedge}\text{N})(\text{POP})]^+$ complexes [13–18]. Significant advances in this area have been achieved through a judicious choice of $\text{N}^{\wedge}\text{N}$ ligands, in particular bulky phenanthroline [13, 14], azolate [11, 15], and bipyridine ligands [16, 17].

Recently, a series of imidazole-fused phenanthroline (Phenanthrolineimidazole, imPhen) ligands have been developed [18, 19] because of their interesting electronic properties and the relative simplicity of their synthesis. A rich variety of functional groups with different electron-donating or electron-accepting properties can be easily functionalized on the imPhen framework. In our previous paper, we reported a series of $\text{Re}(\text{I})$ complexes based on imPhen ligands containing indolyl and thienyl moieties [20, 21]. In this paper, three $[\text{Cu}(\text{N}^{\wedge}\text{N})(\text{POP})]^+$ complexes incorporating imPhen derivatives and POP as ligands were synthesized and characterized (Fig. 1). The addition of phenyl, naphthyl, and anthryl moieties with various degrees of π -conjugation and bulkiness on the imidazole ring of the imPhen ligand, is expected to cause significant changes in the photophysical properties of the corresponding $\text{Cu}(\text{I})$ complexes. In this paper, we describe the structural and spectral properties of these complexes. The assignments of the experimental electronic absorption and emission spectra were determined using density functional theory (DFT) and time-dependent density functional theory (TDDFT).

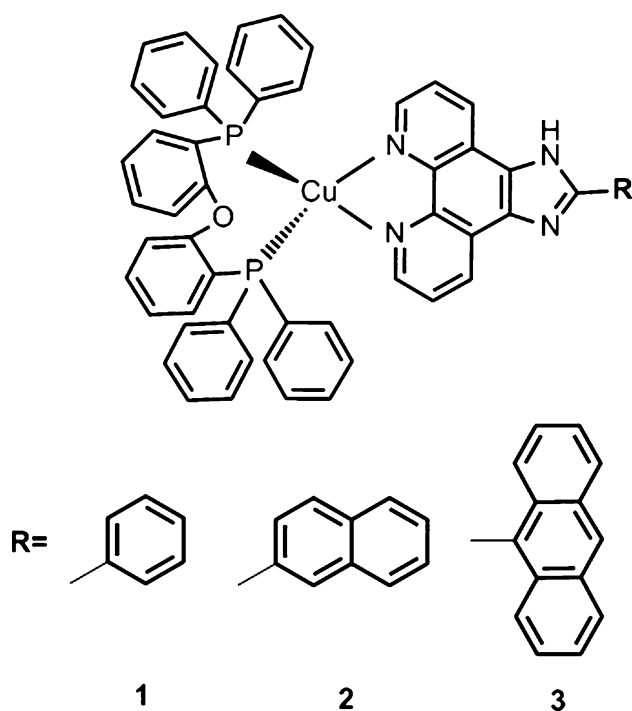


Fig. 1 Molecular structures of the $\text{Cu}(\text{I})$ complexes studied in this study

Experimental

Materials and methods

1,10-phenanthroline (Phen), potassium bromide, benzaldehyde, aniline, ammonium acetate, $[\text{Cu}(\text{CH}_3\text{CN})_4]\text{PF}_6$, and bis[2-(diphenylphosphino)phenyl]ether (POP) were purchased from Aladdin Reagent Co. and used without further purification. Concentrated sulfuric and nitric acids were purchased from Sinopharm Chemical Reagent Co.

^1H NMR spectra were recorded on a Bruker AV400 MHz spectrometer, using tetramethylsilane (TMS) as internal reference. DMSO and CDCl_3 were used as solvents. UV–Vis absorption spectra were measured using a PerkinElmer Lambda-900 spectrophotometer. Fluorescence spectra were determined with a Hitachi F-4500 fluorescence spectrophotometer. Photoluminescence quantum yields (Φ) were measured in poly(methylmethacrylate) (PMMA) films using an absolute photoluminescence yield spectrometer (Quantaury-QY, C11347, Hamamatsu Photonics, Japan). The excited-state lifetimes (τ) were measured using a time-correlated single photon counting (TCSPC) system on a Quantaury-Tau instrument (Hamamatsu Photonics, Japan).

Preparation of 1,10-phenanthroline-5,6-dione

1,10-Phenanthroline-5,6-dione was synthesized according to a modified literature procedure. 1,10-Phenanthroline monohydrate (10 g, 50.4 mmol) was dissolved in 60 mL of concentrated sulfuric acid. Sodium bromide (5.19 g, 50.4 mmol) was then added, followed by 30 mL of 70 wt% nitric acid. The mixture was heated under reflux for 6 h. After 6 h, the temperature was reduced to 95 °C, and the reflux condenser was removed to allow bromine vapors to escape overnight. After cooling, the mixture was poured onto 800 g of ice, carefully neutralized to pH 7 with 10 M sodium hydroxide, and cooled to room temperature. The resulting turbid solution was filtered. The aqueous phase was extracted with CH_2Cl_2 , and the organic phase was dried over anhydrous magnesium sulfate and then evaporated under reduced pressure. The crystalline residue was recrystallized from 300 mL of methanol to give the pure dione. Yield: 57 % (6.0 g). ^1H NMR (400 MHz, CDCl_3): 9.11–9.13 (dd, 2H), 8.50–8.52 (dd, 2H), 7.59–7.61 (dd, 2H).

Preparation of PimP

A mixture of 1,10-phenanthroline-5,6-dione (104 mg, 0.50 mmol), benzaldehyde (72 mg, 0.68 mmol), ammonium acetate (805 mg, 11.3 mmol), and glacial acetic acid

(13 mL) was refluxed for 4 h and then cooled to room temperature. It was diluted with water, and dropwise addition of concentrated aqueous ammonia gave a yellow precipitate, which was collected, washed with water, and dried. The crude product was purified by chromatography on silica gel, eluting with an 8:1 mixture of CH₂Cl₂ and methanol. Yield of 2-phenyl-1*H*-imidazo[4,5-*f*][1,10]phenanthroline (PimP): 96 mg (65 %). ¹H NMR (400 MHz, DMSO): 13.76 (s, 1H), 9.02 (d, *J* = 8.0 Hz, 2H), 8.93 (d, *J* = 8.0 Hz, 2H), 8.29 (d, *J* = 7.9 Hz, 2H), 7.82 (dd, *J* = 7.9, 4.4 Hz, 2H), 7.61 (t, *J* = 7.5 Hz, 2H), 7.51 (t, *J* = 7.2 Hz, 1H).

Preparation of NimP

The synthetic procedure for NimP was the same as that for PimP except that 106 mg (0.68 mmol) 2-naphthaldehyde was used for the reaction. Yield of 2-(2-naphthyl)-1*H*-imidazo[4,5-*f*]phenanthroline (NimP): 95 mg (55 %). ¹H NMR (400 MHz, DMSO-*d*₆): 13.76 (s, 1H), 9.10–9.02 (m, 2H), 8.98 (d, *J* = 7.2 Hz, 2H), 8.83 (s, 1H), 8.45 (d, *J* = 8.5 Hz, 1H), 8.14 (dd, *J* = 16.6, 8.0 Hz, 2H), 8.03 (d, *J* = 8.4 Hz, 1H), 7.86 (dd, *J* = 7.9, 4.2 Hz, 2H), 7.63 (p, *J* = 8.4 Hz, 2H).

Preparation of AimP

The synthetic procedure for AimP was the same as that for PimP except that 140.2 mg (0.68 mmol) 9-anthrylaldehyde was used for the reaction, and the reaction mixture was refluxed for 6 h. Yield of 2-(9-anthryl)-1*H*-imidazo[4,5-*f*]phenanthroline (AimP): 89 mg (45 %). ¹H NMR (400 MHz, DMSO-*d*₆): 14.16 (s, 1H), 9.02 (d, *J* = 4.1 Hz, 2H), 8.90 (d, *J* = 8.1 Hz, 1H), 8.85 (s, 1H), 8.72 (d, *J* = 7.3 Hz, 1H), 8.20 (d, *J* = 8.4 Hz, 2H), 7.79 (dd, *J* = 8.0, 4.4 Hz, 2H), 7.74 (d, *J* = 8.7 Hz, 2H), 7.60–7.52 (m, 2H), 7.52–7.44 (m, 2H).

Preparation of complex 1

A mixture of [Cu(CH₃CN)₄](PF₆) (31 mg, 0.1 mmol), POP (54 mg, 0.1 mmol), and nitrogen-saturated CH₂Cl₂ (10 mL) was stirred for 2 h under a N₂ atmosphere. PimP (30 mg, 0.1 mmol) was then added. The mixture turned yellow instantaneously and then was stirred for 3 h at room temperature. The mixture was filtered with kieselguhr, and the clear red filtrate was evaporated to dryness. The resulting yellow solid was recrystallized with diethyl ether from CH₂Cl₂. Yield: 50 mg (42 %). ¹H NMR (400 MHz, DMSO) 9.09 (d, *J* = 8.1 Hz, 2H), 8.78 (d, *J* = 8.0 Hz, 2H), 8.34 (d, *J* = 7.8 Hz, 2H), 7.91–7.82 (m, 2H), 7.61 (t, *J* = 7.2 Hz, 2H), 7.52 (d, *J* = 7.3 Hz, 1H), 7.44 (t, *J* = 7.5 Hz, 2H), 7.30 (t, *J* = 7.1 Hz, 5H), 7.19 (t, *J* = 7.3 Hz, 9H), 7.09 (t, *J* = 7.3 Hz, 2H), 6.97 (d, *J* = 5.7 Hz, 8H), 6.63 (s, 2H).

Preparation of complex 2

The synthetic procedure for complex 2 was the same as that for complex 1. The complex was isolated as a yellow solid. Yield: 37 mg (42 %). ¹H NMR (400 MHz, DMSO-*d*₆): 9.11 (d, *J* = 8.3 Hz, 2H), 8.84 (d, *J* = 29.5 Hz, 3H), 8.50 (d, *J* = 8.0 Hz, 1H), 8.13 (s, 2H), 8.02 (d, *J* = 7.0 Hz, 1H), 7.88 (s, 2H), 7.62 (s, 2H), 7.45 (t, *J* = 7.4 Hz, 2H), 7.31 (t, *J* = 7.2 Hz, 4H), 7.26 (s, 1H), 7.20 (t, *J* = 7.4 Hz, 8H), 7.10 (t, *J* = 7.3 Hz, 3H), 6.99 (d, *J* = 5.9 Hz, 8H), 6.65 (s, 2H).

Preparation of complex 3

The synthetic procedure for complex 3 was the same as that for complex 1. The complex was isolated as a yellow solid. Yield: 40 mg (42 %). ¹H NMR (400 MHz, DMSO) δ 9.19 (s, 1H), 9.19 (s, 1H), 8.95 (s, 1H), 8.79 (s, 2H), 8.16 (s, 2H), 7.98 (s, 1H), 7.79 (s, 2H), 7.52 (dd, 10H), 7.30 (d, 14H), 7.07 (d, 8H), 6.70 (s, 2H).

DFT calculations

All calculations were performed using the Gaussian 09 [22] program package. The B3LYP exchange-correlation function [23, 24] was used to optimize the ground-state geometries of complexes 1–3 using the polarized continuum model (PCM) in CH₂Cl₂ medium. The 6-31G* basis set [25, 26] was used on the C, H, N, O, and P atoms, and the LANL2DZ basis set [27] was adopted for the Cu atoms. The unrestricted B3LYP method was used to optimize the lowest triplet state geometries (T₁) with the PCM solvent method in toluene.

Using the optimized ground geometries, the TDDFT method [28, 29] with PCM [30] in CH₂Cl₂ medium at the same level of theory was used to simulate the absorption spectra of complexes 1–3. The first 100 singlet vertical excitations were obtained from the TDDFT output file to construct the calculated absorption spectra. Calculated electronic density plots for the frontier molecular orbitals were prepared using Gauss View 4.1.2 software, and the spin-density populations were calculated using Multiwfn analyzer software [31].

Results and discussion

Synthesis

The synthetic pathways for the free ligands and their Cu(I) complexes are shown in Scheme 1. 1,10-Phenanthroline-5,6-dione was synthesized according to a modified literature procedure [32]. The free ligands were prepared

by a condensation reaction according to the literature procedure [33]. Complexes **1–3** were prepared by the conventional reactions of $[\text{Cu}(\text{CH}_3\text{CN})_4]\text{BF}_6$ with one equivalent of the POP ligand and one equivalent of the corresponding imPhen derivative ligand.

UV–Vis and photoluminescence spectra

Figure 2 shows the UV–Vis spectra of complexes **1–3** in CH_2Cl_2 solution at room temperature, and the absorption band maxima are listed in Table 1. A high-lying absorption band of complex **1** localized at 282 nm with a distinct shoulder at around 306 nm is observed, which can be provisionally assigned to the ligand-centered $\pi \rightarrow \pi^*$ transitions of the imPhen and POP ligands. At longer wavelengths (360–520 nm), weak and long tails centered at approximately 409 nm are present, which are not visible in the free ligand spectra (not shown). These low-energy absorption bands are assigned to metal-to-ligand charge transfer (MLCT) transitions [$d(\text{Cu}) \rightarrow \pi^*(\text{imPhen})$] mixed with ligand-to-ligand charge transfer [LLCT, $\pi(\text{POP}) \rightarrow \pi^*(\text{imPhen})$] transitions. In the case of complex **2**, the highest lying absorption band localized at 274 nm is much broader than that of complex **1**, indicating that this band has a different transition character compared to complex **1**. This band may be assigned to an intra-ligand charge transfer [ILCT, $\pi(\text{POP}) \rightarrow \pi^*(\text{POP})$] transition with large MLCT character, which is supported by TDDFT calculations. In addition, a broad plateau is observed in the range of 310–330 nm, assigned to the combined contributions of multiconfigurational transitions involving the POP ligand, imPhen ligand, and naphthyl moiety. The TDDFT calculations suggest that a large MLCT contribution is responsible for these bands. A weak MLCT absorption band centered at 420 nm is also observed (see inset Fig. 2). This band is red-shifted by 11 nm compared to that of complex **1**, owing to the decrease in HOMO–LUMO energy gap resulting from the extended π -conjugation of the N^N

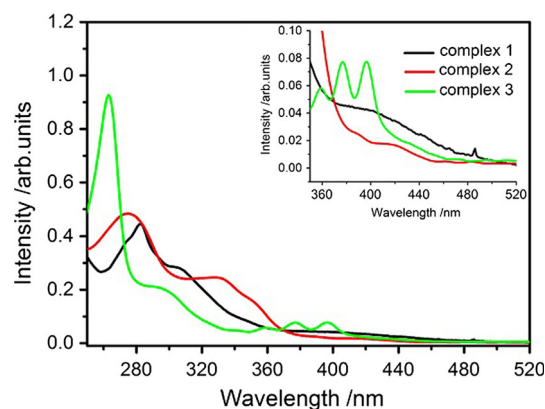


Fig. 2 Absorption spectra in dichloromethane at 298 K of complexes **1–3**. (Inset) the region of 350–520 nm is magnified to allow easy comparison

ligand due to the introduction of the naphthyl moiety. The spectrum of complex **3** shows the highest lying band at around 264 nm with a shoulder at 301 nm. The 264-nm band is assigned to the ligand-centered $\pi \rightarrow \pi^*$ transitions of the anthracene group, while the shoulder is more complicated and arises from a mixture of transition characters. It is worth noting that the additional anthracene absorption band is also observed in the visible region range from 350 to 410 nm in the spectrum of complex **3** (see inset Fig. 2), which retains its vibronic fine structure, implying only weak conjugation between the imPhen ring and anthracene group. This may be ascribed to the larger torsion angle between these rings. Additionally, weak tails centered at 435 nm are observed, which can be assigned to LLCT [$\pi(\text{Anth}) \rightarrow \pi^*(\text{imPhen})$] transitions.

The normalized emission spectra of complexes **1–3** are shown in Fig. 3 as obtained from thin solid films of PMMA in which 20 % by weight of the complex was dispersed. The associated emission parameters are listed in Table 1. Complexes **1** and **2** show similar emission properties with broad and structureless features, suggesting that these

Scheme 1 Synthetic pathways of the ligands and Cu(I) complexes

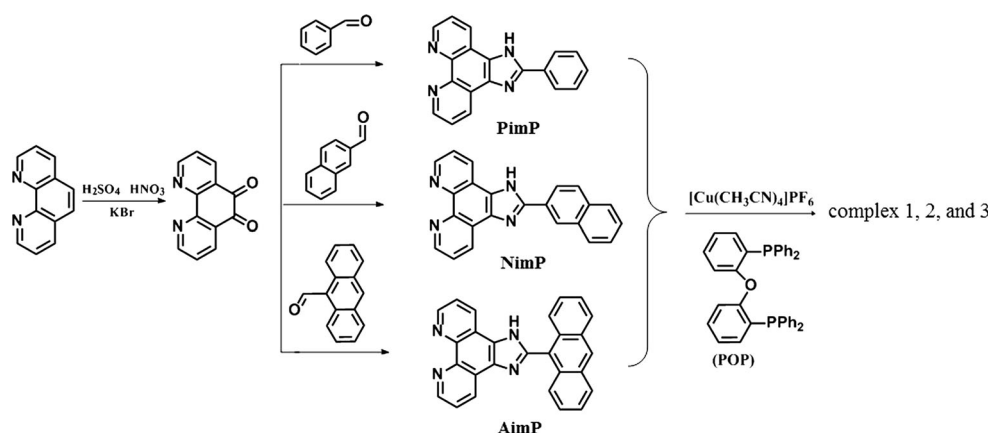


Table 1 Photophysical properties of complexes 1–3

Complex	λ_{abs} (nm)	λ_{em} (nm)	τ (μs)	Φ (%)	k_r (10^4 s^{-1})	k_{nr} (10^4 s^{-1})
1	401	570	4.24	4.3	1.01	22.6
2	420	593	5.04	3.5	0.69	19.1
3	435	552	1.53	0.2	1.30	65.2

emissions could be assigned to the triplet $^3\text{MLCT}$ character with some $^3\text{LLCT}$ character. Complex **3** exhibits a larger blueshift emission, clearly indicating an emitting triplet state of predominant $^3\text{LLCT}$ character. The emission maximum at 593 nm of complex **2** is red-shifted by 23 nm compared to complex **1** (λ_{max} 570 nm), which can be rationalized by the larger degree of π -conjugation in complex **2** compared to complex **1**, revealing a good correlation with respect to the lowest lying $^1\text{MLCT}$ absorption band of these complexes as discussed above.

The different nature of the emitting states is also reflected in the photoluminescence quantum yields (PLQY) and in excited-state lifetimes. In PMMA films, complexes **1** and **2** give PLQYs of 4.3 and 3.5 %, respectively. These values are much larger than that of complex **3** (PLQY 0.2 %). The excited-state lifetimes of complexes **1** and **2** in PMMA films (4.24 and 5.04 μs , respectively) are much longer than that of complex **3** (1.53 μs). The calculated radiative decay rates (K_r) of complexes **1**, **2**, and **3** are 1.01×10^4 , 0.69×10^4 , 1.30×10^4 , respectively, whereas their calculated nonradiative decay rates (K_{nr}) are 22.6×10^4 , 19.1×10^4 , 65.2×10^4 , respectively. The K_{nr} value of complex **3** is two times larger than those of complexes **1** and **2**, which is due to the change in the nature

of the triplet state (T_1) from a $^3\text{MLCT}/^3\text{LLCT}$ transition (complexes **1** and **2**) to a more $^3\text{LLCT}$ transition.

Ground-state geometries and molecular orbital properties

The optimized ground-state geometric structures for the complexes are shown in Fig. 4, and selected bond lengths and angles are summarized in Table 1S in the Supporting Information. Vibrational frequencies were calculated based on these optimized geometries to verify that the geometries represented a minimum on the potential energy surface. The angle between the N2Cu1N3 and P1Cu1P2 planes is 88.4° , 89.3° , and 86.8° for complexes **1**, **2**, and **3**, respectively, suggesting slightly distorted pseudotetrahedral geometries. The N1–C1–C2–C3 dihedral angle displays significant variability (10.1° for complex **1**, 9.2° for complex **2**, and 58.4° for complex **3**; see Fig. 4 for the atom numbering). This can be explained by the steric repulsion between the atom H1 of the imidazole ring and atom H2 of the aryl substituent. These angular variations are probably responsible for the difference in their photophysical properties.

Figure 5 shows the energy levels and atomic orbital compositions calculated for the HOMO and LUMO of complexes 1–3 including solvent effects. It is clear that the substituent (phenyl, naphthyl, or anthryl) at position C2 has a significant effect on the composition of the HOMO. The HOMO is mainly localized on Cu and the POP ligands, with some contribution from the imPhen moieties for complex **1**. The HOMO of complex **2** is similar to that of complex **1**, but also includes a contribution from the naphthyl moiety, which slightly destabilizes the HOMO of complex **2** compared to that of complex **1**. With respect to complex **3**, the HOMO is mainly localized on the anthryl moiety. The main reason for this different composition from complexes **1** to **3** is attributed to the torsion angle of 58.4° between the anthryl moiety and the imPhen ring, which largely breaks π -conjugation between these ring systems. On the other hand, the LUMO of all three complexes is predominately localized on the imPhen group, which is hardly influenced by different substituents on the N^N ligands. Consequently, the LUMO appears at very similar energies for **1** (-2.30 eV), **2** (-2.31 eV), and **3** (-2.32 eV). Additionally, the calculated HOMO–LUMO energy gap follows the order: **1** > **2** > **3**, in reasonably

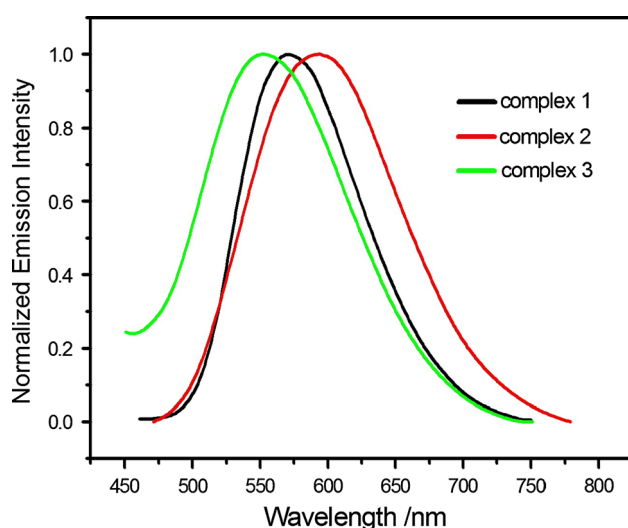


Fig. 3 Normalized emission spectra of complexes 1–3 in PMMA films

Fig. 4 Optimized ground-state geometric structures of complexes 1–3

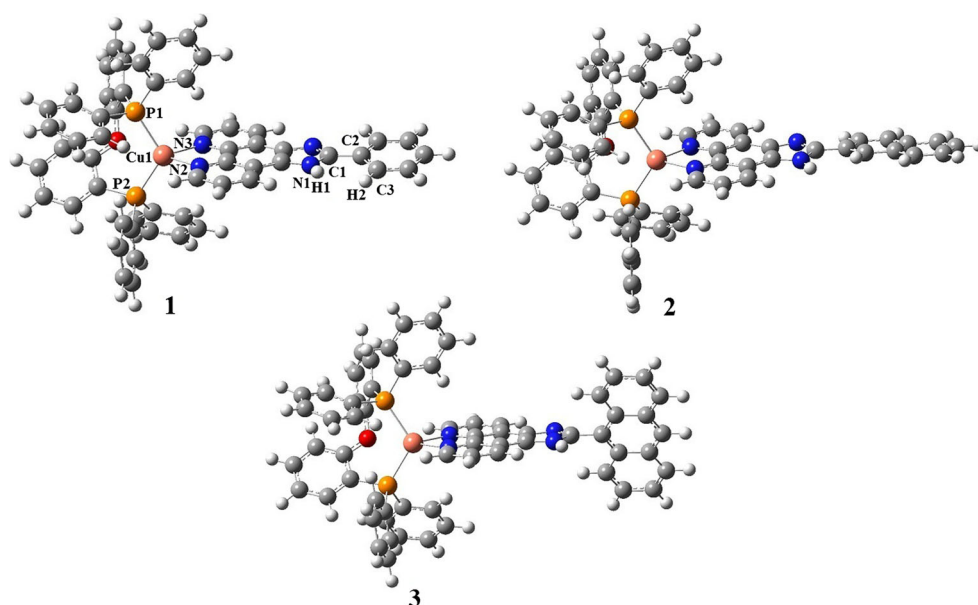
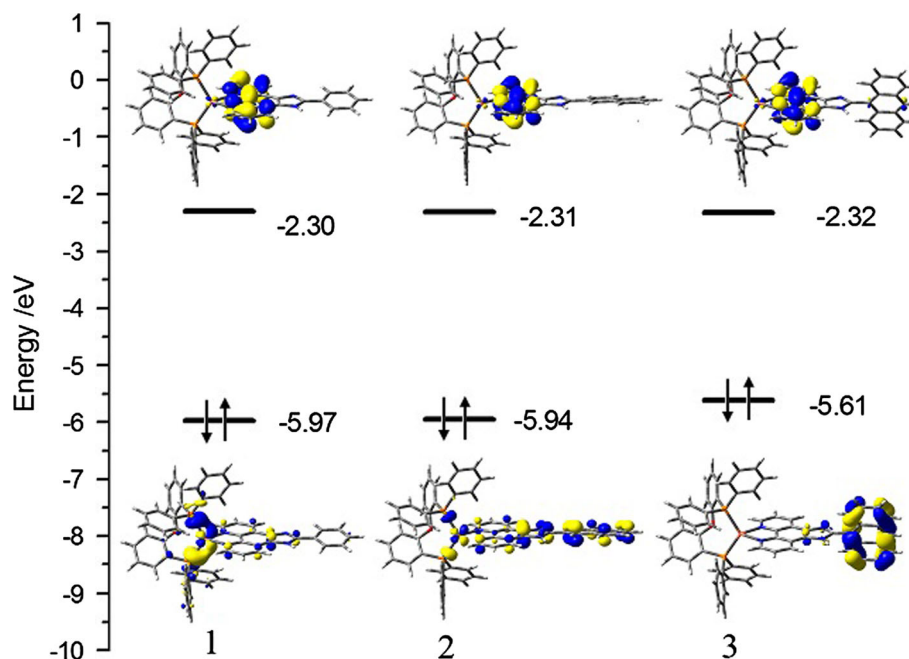


Fig. 5 Energy diagram and the energy values calculated for the HOMO and LUMO of complexes 1–3



good agreement with the red shift of the lowest energy absorption maxima observed in the experiments.

Theoretical absorption spectra

To gain insight into the character of UV–Vis transitions of these the complexes, TDDFT calculations were undertaken to simulate their absorption spectra. Table 2 lists the dominant singlet–singlet vertical excitations, their oscillator strengths, assignment configurations, and excitations with maximum coefficients for each of the complexes. To

conveniently discuss the character of the electronic transitions, the frontier molecular orbital compositions of the complexes in CH_2Cl_2 solution, expressed in terms of the four molecular fragments, are shown in Table 2–4S (see Supporting Information). A comparison of calculated and experimental absorption spectra for the complexes is presented in Fig. 6. In general, the experimental spectra are well reproduced by the calculations.

For complex 1, we calculate an intense feature at 275 nm, together with a shoulder at 304 nm, in good agreement with the 282 and 306 nm experimental values. The absorption

Table 2 Electronic absorptions of complexes **1–3** in CH₂Cl₂ based on TDDFT calculations at the (B3LYP)/6-31 g*/LANL2DZ level, together with the experimental values

Complex	Excited state	Transition	Coeff.	<i>E</i> (eV/nm)	Oscillator strength	Assign	Exptl. (nm)
1	1	H → L	0.69621 (96.9 %)	3.05/406	0.1696	MLCT/LLCT/ILCT	402
	6	H - 1 → L + 1	0.64004 (81.9 %)	3.66/338	0.2182	LLCT/ILCT	
	12	H - 1 → L + 2	0.66186 (87.6 %)	4.08/304	0.6576	ILCT/LLCT	306
	27	H - 2 → L + 3	0.44943 (40.4 %)	4.46/278	0.1532	MLCT/ILCT	
		H - 3 → L + 3	-0.38967 (30.4 %)			MLCT/LLCT	
	30	H - 5 → L + 1	0.37488 (28.1 %)	4.51/275	0.2606	ILCT	282
H - 10 → L		-0.34406 (23.7 %)			LLCT		
2	1	H → L	0.65544 (86.0 %)	3.04/408	0.2251	MLCT/LLCT/ILCT	420
	6	H - 1 → L + 1	0.58492 (68.4 %)	3.51/353	0.3691	MLCT/LLCT	
		H → L + 1	-0.34405 (23.7 %)			MLCT/LLCT/ILCT	
	9	H → L + 2	0.65837 (86.7 %)	3.78/328	0.3659	ILCT/LLCT/MLCT	328
	12	H - 1 → L + 2	0.56153 (63.1 %)	3.91/317	0.3145	LLCT/MLCT	
		H - 3 → L + 1	0.30717 (18.9 %)			LLCT/ILCT	
	32	H - 2 → L + 3	0.49175 (48.4 %)	4.48/277	0.3780	MLCT/ILCT	274
		H - 6 → L + 1	0.21539 (13.1 %)			ILCT/LLCT	
	34	H - 12 → L	0.31838 (20.3 %)	4.50/275	0.2737	LLCT	
		H - 11 → L	0.29394 (17.3 %)			LLCT	
H - 4 → L + 3		-0.26483 (14.0 %)			MLCT/ILCT		
3	1	H → L	0.68935 (95.0 %)	2.88/431	0.1198	LLCT	435
	2	H → L + 1	0.68319 (93.3 %)	3.03/410	0.3084	LLCT	
	14	H → L + 5	0.46335 (42.9 %)	3.95/314	0.0746	LLCT	
		H → L + 4	0.45076 (40.6 %)			LLCT	
	39	H - 3 → L + 3	0.38878 (30.2 %)	4.46/278	0.1116	MLCT/LLCT	301
		H - 7 → L + 1	0.32927 (21.7 %)			ILCT	
	42	H - 2 → L + 3	0.34071 (23.2 %)	4.50/275	0.1895	MLCT/ILCT	
		H - 7 → L	-0.27625 (15.3 %)			ILCT	
	82	H → L + 9	0.35801 (25.6 %)	4.89/254	0.6709	ILCT	264
H - 6 → L + 1		0.28093 (15.8 %)			ILCT		

MLCT metal-to-ligand charge transfer, LLCT ligand-to-ligand charge transfer, ILCT intra-ligand charge transfer

peak at 275 nm mainly originates from the mixed transitions of HOMO - 5 → LUMO + 1 (28.1 %) and HOMO - 10 → LUMO (23.7 %). HOMO - 5 and HOMO - 10 mainly consist of $\pi(\text{imPhen})$ (76.33 %) and $\pi(\text{POP})$ (92.85 %), respectively, while the LUMO and LUMO + 1 are predominantly composed of $\pi^*(\text{imPhen})$ (see Supporting Information). Thus, this band can be assigned to a combination of LLCT and ILCT. The 304-nm shoulder originates from the transition of HOMO - 1 → LUMO + 2, which can be ascribed to $[\pi(\text{imPhen}) + \pi(\text{Ph})] \rightarrow [\pi^*(\text{imPhen}) + \pi^*(\text{Ph})]$ with LLCT/ILCT character. At longer wavelengths, the calculated lowest lying absorption band localized at 406 nm, corresponding to the weaker absorption peak at 402 nm observed in the experimental spectrum, should be assigned to the HOMO → LUMO transition

originating from $[\text{d}(\text{Cu}) + \pi(\text{POP}) + \pi(\text{imPhen})] \rightarrow [\pi^*(\text{imPhen})]$ with mixed MLCT/LLCT/ILCT character.

The highest lying absorption band of complex **2** calculated at 277 nm, which corresponds well to the experimental value of 274 nm, appears to mainly originate from the transition of HOMO - 2 $[\text{d}(\text{Cu}) + \pi(\text{POP})] \rightarrow \text{LUMO} + 3$ $[\pi^*(\text{POP})]$ (48.4 %) with MLCT/ILCT character. Additionally, mixed transitions of HOMO - 4/HOMO - 11/HOMO - 12 → LUMO/LUMO + 3 with LLCT/MLCT/ILCT character may be responsible for this band. The excited state 9 originated from the HOMO $[\text{d}(\text{Cu}) + \pi(\text{POP}) + \pi(\text{imPhen}) + \pi(\text{Naph})] \rightarrow \text{LUMO} + 2$ $[\pi^*(\text{imPhen}) + \pi^*(\text{Naph})]$ transition with MLCT/LLCT/ILCT character and the excited state 12 at 317 nm originated from the HOMO - 1 $[\text{d}(\text{Cu}) + \pi(\text{POP})] \rightarrow \text{LUMO} + 2$ $[\pi^*(\text{imPhen}) + \pi^*(\text{Naph})]$ with the

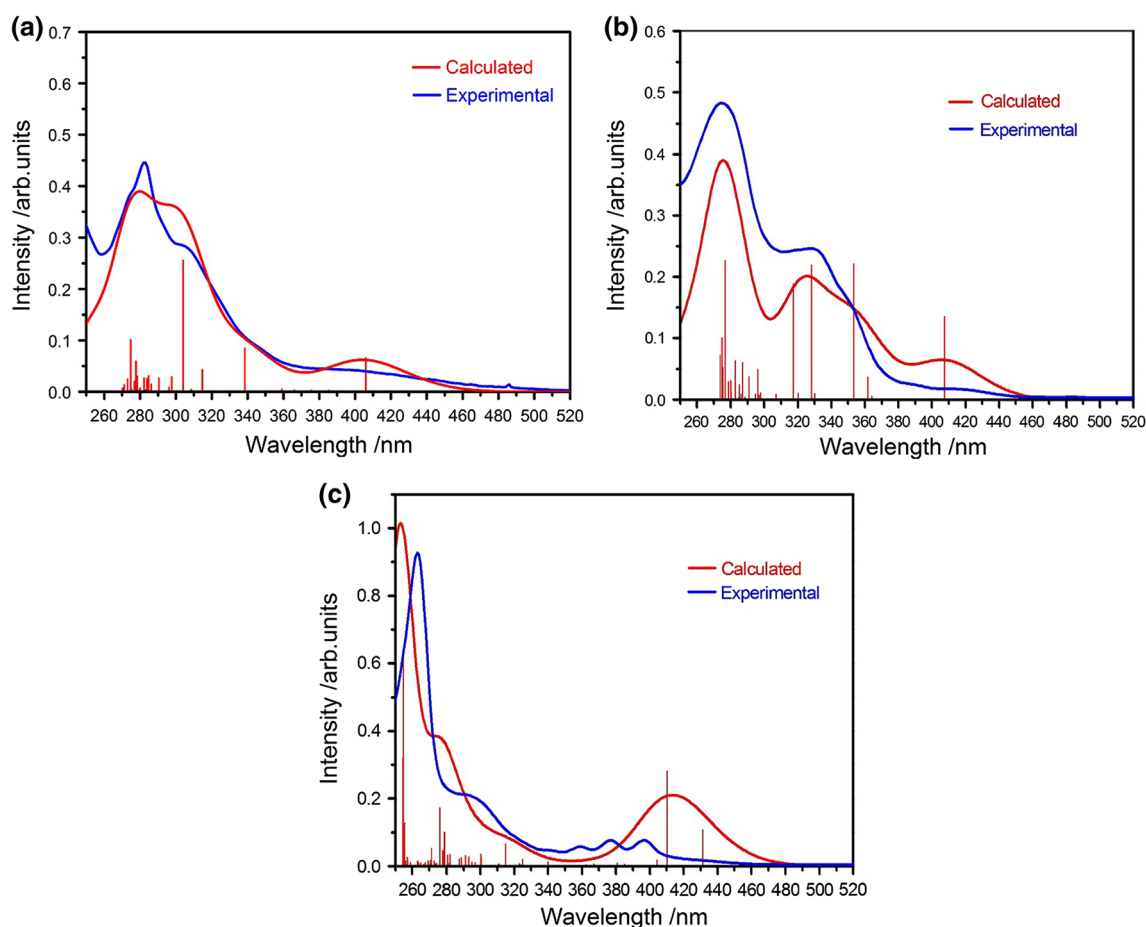


Fig. 6 Comparison of the calculated (red line) and experimental (blue line) absorption spectra in CH_2Cl_2 solution for complex **1** (a); complex **2** (b); complex **3** (c). Red vertical lines correspond to oscillator strength of calculated singlet-singlet transitions. (Color figure online)

character of MLCT/LLCT responsible for the broad shoulder centered at 327 nm, in good agreement with the experimental value of 328 nm. The calculated lowest lying absorption band localized at 408 nm, corresponding to the weaker absorption peak at 420 nm observed in the experimental spectrum, should be assigned to the HOMO $[\text{d}(\text{Cu}) + \pi(\text{POP}) + \pi(\text{imPhen}) + \pi(\text{Naph})] \rightarrow \text{LUMO} [\pi^*(\text{imPhen})]$ transition with MLCT/LLCT/ILCT character.

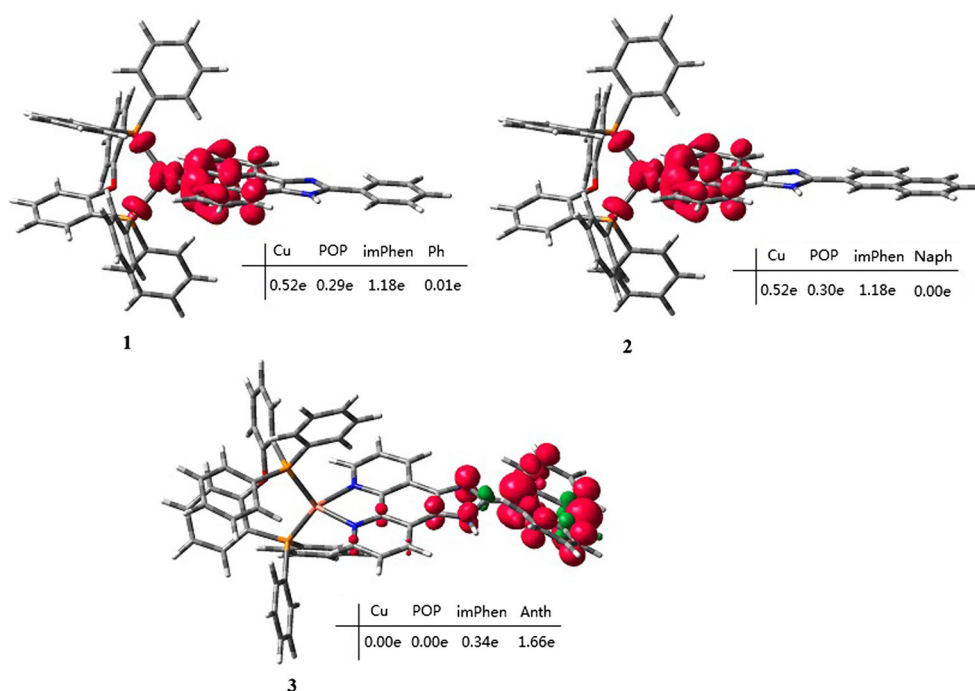
With respect to complex **3**, the calculated highest lying absorption band at 254 nm, corresponding to the experimentally observed band at 264 nm, is dominated by the HOMO $[\pi(\text{Anth})] \rightarrow \text{LUMO} + 9 [\pi^*(\text{Anth})]$ transition (25.6 %) and HOMO-6 $[\pi(\text{Anth})] \rightarrow \text{LUMO} + 1 [\pi^*(\text{Anth})]$ (15.8 %) with ILCT character. The experimentally observed shoulder at 304 nm originates from the combined contributions of the excited state 39 at 278 nm and excited state 42 at 275 nm. The HOMO - 3 $[\text{d}(\text{Cu}) + \pi(\text{imPhen})] \rightarrow \text{LUMO} + 3 [\pi^*(\text{POP})]$ (MLCT/LLCT) and HOMO - 7 $[\pi(\text{imPhen})] \rightarrow \text{LUMO} + 1 [\pi^*(\text{imPhen})]$ (ILCT) excitations are the main configuration for excited state 39, while the transition configuration of

HOMO - 2 $[\text{d}(\text{Cu}) + \pi(\text{POP})] \rightarrow \text{LUMO} + 3 [\pi^*(\text{POP})]$ (MLCT/ILCT) mainly contributes to excited state 42. The calculated absorption band with the largest oscillator strength ($f = 0.3084$) is localized at 410 nm, which predominately originates from the HOMO $[\pi(\text{Anth})] \rightarrow \text{LUMO} + 1 [\pi^*(\text{Anth})]$ transition with ILCT character, corresponding well to the experimental bands in the range of 350–410 nm considering the rather limited dimensions of the basis set and the approximate nature of solvent model. The weak absorption band centered at 435 nm in the experimental spectrum, which was well overlapped with the $\pi-\pi^*$ absorption of anthracene, can be assigned to the transition configuration of HOMO $[\pi(\text{Anth})] \rightarrow \text{LUMO} [\pi^*(\text{imPhen})]$ with LLCT character based on the calculated absorption band at 431 nm.

Triplet excited states and emission properties

To gain insight into the nature of the emission properties of the complexes, their lowest lying triplet excited-state geometries (T_1) were optimized at the spin-unrestricted

Fig. 7 Spin density distribution contours (isovalue = 0.004) for the lowest triplet state T_1 of complexes **1–3**. The values of the unpaired electron spin-density population are depicted together with the electronic nature of the states



UB3LYP/6-31G*/LANL2DZ level with a spin multiplicity of 3. The optimized lowest triplet state structures and selected geometric parameters are provided in Figure 2S and Table 1S in the Supporting Information. Where stated, toluene was chosen as the solvent, since its polarity is comparable with that of the doped PMMA films. A substantial decrease in the intersection angle of $N_2Cu_1N_3$ and $P_1Cu_1P_2$ planes is observed for complexes **1** and **2** because of the presence of Jahn–Teller distortion. In addition, the Cu–P bonds lengthen by about 0.06–0.1 Å for complexes **1** and **2** compared to S_0 , whereas the Cu–N bonds shorten by about 0.135–0.158 Å due to the electronic transfer from the Cu and POP ligand to the imPhen ligand. Additionally, the phenyl and naphthyl groups are coplanar with the phenanthrolineimidazole ligand in the excited state. For complex **3**, the Cu–P and Cu–N bond lengths, as well as the dihedral angle between the $N_2Cu_1N_3$ and $P_1Cu_1P_2$ planes in the excited state are not significantly different to those in the ground state, suggesting little to no contribution of the Cu atom and POP ligand in the T_1 state. On the other hand, the coplanarity within the anthryl and imidazole rings is substantially distorted because of the steric repulsion between H1 of the imidazole ring and H2 of the anthryl substituent.

The nature of the emitting excited state of each complex can be identified by the unpaired electron spin-density distribution, as shown in Fig. 7. For complex **1**, the unpaired electron spin-density distribution in the T_1 state (Cu, 0.52e; POP, 0.29e; imPhen, 1.18e; Ph, 0.01e) confirms the emission behavior to be of ${}^3MLCT/{}^3LLCT$ character and illustrates the higher contribution of the d(Cu) to the imPhen ligand

with some contribution of the POP ligand to the imPhen ligand. A similar spin-density distribution is observed for complex **2** in the T_1 state (Cu, 0.52e; POP, 0.30e; imPhen, 1.18e; Naph, 0.00e), and the ${}^3MLCT/{}^3LLCT$ characters are responsible for the T_1 state of complex **2**. With respect to **3**, the spin-density distribution completely differs from that of complexes **1** and **2**. The spin densities calculated for T_1 (Cu, 0.00e; POP, 0.00e; imPhen, 0.34e; Anth, 1.66e) undoubtedly confirm the dominant 3LLCT nature from the imPhen ligand to anthryl group.

Conclusions

Three copper(I) complexes, containing the imidazo[4,5-f]-[1,10]-phenanthroline ligand with phenyl, naphthyl, and anthryl groups, respectively, were synthesized and characterized. The profound differences in absorption and luminescence properties of the complexes are consistent with the results of DFT and TDDFT calculations. These experimental and theoretical insights should provide some insights into the design and synthesis of efficient luminescent copper(I) complexes.

Acknowledgments The work was supported by the National Natural Science Foundation of China (Nos. 21462020 and 21443010), Jiangxi Science and Technology Normal University Key Laboratory of Organic–Inorganic Composite Materials (Key training base), and the Natural Science Foundation of Jiangxi Province (No. 20151BAB203006). The authors thank the Guizhou University High Performance Computation Chemistry Laboratory (GHPCC) for help with computational studies.

References

1. McMillin DR, Buckner MT, Ahn BT (1977) *Inorg Chem* 16:943. doi:10.1021/ic50170a046
2. Funaki T, Funakoshi H, Kitao O, Onozawa-Komatsuzaki N, Kasuga K, Sayama K, Sugihara H (2012) *Angew Chem Int Ed* 51:7528. doi:10.1002/anie.201108738
3. Bolink HJ, Cappelli L, Coronado E, Gavina P (2005) *Inorg Chem* 44:5966. doi:10.1021/ic0507058
4. Wong KMC, Chan MMY, Yam VWW (2014) *Adv Mater* 26:5558. doi:10.1002/adma.201306327
5. Cunningham CT, Cunningham KLH, Michalec JF, McMillin DR (1999) *Inorg Chem* 38:4388. doi:10.1021/ic9906611
6. Felder D, Nierengarten JF, Barigelletti F, Ventura B, Armaroli N (2001) *J Am Chem Soc* 123:6291. doi:10.1021/ja0043439
7. Kern JM, Sauvage JP, Weidmann JL, Armaroli N, Flamigni L, Ceroni P, Balzani V (1997) *Inorg Chem* 36:5329. doi:10.1021/ic970707v
8. McCusker CE, Castellano FN (2013) *Inorg Chem* 52:8114. doi:10.1021/ic401213p
9. Femoni C, Muzzioli S, Palazzi A, Stagni S, Zacchini S, Monti F, Accorsi G, Bolognesi M, Armaroli N, Massi M, Valenti G, Marcaccio M (2013) *Dalton Trans* 42:997. doi:10.1039/c2dt32056h
10. Nishikawa M, Sawamura S, Haraguchi A, Morikubo J, Takao K, Tsubomura T (2015) *Dalton Trans* 44:411. doi:10.1039/c4dt03176h
11. Chen JL, Cao XF, Wang JY, He LH, Liu ZY, Wen HR, Chen ZN (2013) *Inorg Chem* 52:9727. doi:10.1021/ic4002829
12. Cuttall DG, Kuang SM, Fanwick PE, McMillin DR, Walton RA (2002) *J Am Chem Soc* 124:6. doi:10.1021/ja012247h
13. Armaroli N, Accorsi G, Holler M, Moudam O, Nierengarten JF, Zhou Z, Wegh RT, Welter R (2006) *Adv Mater* 18:1313. doi:10.1002/adma.20052365
14. Zhang QS, Zhou QG, Cheng YX, Wang LX, Ma DG, Jing XB, Wang FS (2006) *Adv Funct Mater* 16:1203. doi:10.1002/adfm.200500691
15. Chi Y, Tong BH, Chou PT (2014) *Coord Chem Rev* 281:1. doi:10.1016/j.ccr.2014.08.012
16. Linfoot CL, Richardson P, Hewat TE, Moudam O, Forde MM, Collins A, White F, Robertson N (2010) *Dalton Trans* 39:8945. doi:10.1039/c0dt00190b
17. Linfoot CL, Leidl MJ, Richardson P, Rausch AF, Chepelin O, White FJ, Yersin H, Robertson N (2014) *Inorg Chem* 53(2014):10854. doi:10.1021/ic500889s
18. Chao H, Li RH, Ye BH, Li H, Feng XL, Cai JW, Zhou JY, Ji LN (1999) *J Chem Soc Dalton Trans*. doi:10.1039/a905790k
19. Cardinaels T, Ramaekers J, Nochemann P, Driesen K, Hecker KV, Meervelt LV, Lei SB, Feyter SD, Guillon D, Donnio B, Binnemans K (2008) *Chem Mater* 20:1278. doi:10.1021/cm070637i
20. Zhao F, Wang JX, Wang YB (2012) *Inorg Chim Acta* 387:100. doi:10.1016/j.ica.2012.01.001
21. Wang JX, Xia HY, Liu WQ, Zhao F, Wang YB (2013) *Inorg Chim Acta* 394:92. doi:10.1016/j.ica.2012.07.032
22. Frisch MJ, Trucks GW, Schlegel HB, Scuseria GE, Robb MA, Cheeseman JR, Scalmani G, Barone V, Mennucci B, Petersson GA, Nakatsuji H, Caricato M, Li X, Hratchian HP, Izmaylov AF, Bloino J, Zheng G, Sonnenberg JL, Hada M, Ehara M, Toyota K, Fukuda R, Hasegawa J, Ishida M, Nakajima T, Honda Y, Kitao O, Nakai H, Vreven T, Montgomery JA Jr, Peralta JE, Ogliaro F, Bearpark M, Heyd JJ, Brothers E, Kudin KN, Staroverov VN, Kobayashi R, Normand J, Raghavachari K, Rendell A, Burant JC, Iyengar SS, Tomasi J, Cossi M, Rega N, Millam NJ, Klene M, Knox JE, Cross JB, Bakken V, Adamo C, Jaramillo J, Gomperts R, Stratmann RE, Yazyev O, Austin AJ, Cammi R, Pomelli C, Ochterski JW, Martin RL, Morokuma K, Zakrzewski VG, Voth GA, Salvador P, Dannenberg JJ, Dapprich S, Daniels AD, Farkas Ö, Foresman JB, Ortiz JV, Cioslowski J, Fox DJ (2009) *Gaussian 09*, revision A. 1. Gaussian, Wallingford
23. Runge E, Gross EK (1984) *Phys Rev Lett* 52:997. doi:10.1103/physrevlett.52.997
24. Mayo SL, Olafson BD, Goddard WA (1990) *J Phys Chem* 94:8897. doi:10.1021/j100389a010
25. Hariharan PC, Pople JA (1974) *Mol Phys* 27:209. doi:10.1080/00268977400100171
26. Gordon MS (1980) *Chem Phys Lett* 76:163. doi:10.1016/0009-2614(80)80628-2
27. Hay PJ, Wadt WR (1985) *J Chem Phys* 82:270. doi:10.1063/1.448799
28. Casida ME, Jamorski C, Casida KC, Salahub DR (1998) *J Chem Phys* 108:4439. doi:10.1063/1.475855
29. Stratmann RE, Scuseria GE, Frisch MJ (1998) *J Chem Phys* 109:8218. doi:10.1063/1.477483
30. Perdew JP, Burke K, Ernzerhof M (1997) *Phys Rev Lett* 78:1396. doi:10.1103/PhysRevLett.78.1396
31. Lu T, Chen FW (2012) *J Comput Chem* 33:580. doi:10.1002/jcc.22885
32. Hiort C, Lincoln P, Norden B (1993) *J Am Chem Soc* 115:3448. doi:10.1021/ja00062a007
33. Wang QM, Tamiaki H (2009) *J Photochem Photobiol A* 206:124. doi:10.1016/j.jphotochem.2009.05.024